



## Effect of Ag-doping on the thermal features of hydroxyapatite

S. Mohamed\*, H. Kamal, Y.M. Moustafa, and M.I. Abdelghany

Glass Research Group, Physics Department, Faculty of Science, Mansoura University, Mansoura 35516, Egypt



CrossMark

### Abstract

A series of Ag-doped hydroxyapatite (Ag-HA) of the general molecular formula  $(Ca_{10-x}Ag_x(PO_4)_6(OH)_2)$ , where  $x = 0, 0.4, 0.8, 1.2,$  and  $1.6$  mole had been prepared by a solution technique. X-ray diffraction (XRD), Fourier transform infrared spectrometry (FTIR), Transmission electron microscope (TEM), Electron diffraction (EDP) and Scanning electron microscope-energy dispersive X-ray spectroscopy (SEM-EDS) were used for assigning the presence of glass-ceramic, crystalline, and polycrystalline phases. Addition of low content of silver to the HA leads to the formation of beta-tricalcium phosphate ( $\beta$ -TCP) and Ag-HA. The spectral changes were directly dependent on Ag concentration, time, and heat treatment temperature. The results revealed the occurrence of different functional groups of HA and  $\beta$ -TCP in the matrices of the glass-ceramic. The role of the nucleating agent Ag was critically assigned and the presence of the characteristic phases of HA and  $\beta$ -TCP was confirmed and properly assigned and addressed. TEM and SEM were used to properly assign the morphology of the formed phases. Ag-HA prepared with  $\beta$ -TCP components can be used as unique bio-ceramic materials in different biological applications.

**Keywords:** Hydroxyapatite,  $\beta$ -TCP, Ag-HA, glass-ceramic, solution technique.

### 1. Introduction

Ceramic materials that are modified to be utilized as medical and dental implants are described as bio-ceramics. Bio-ceramics can function as joint or tissue replacements and as coatings to improve their biocompatibility and corrosion resistance [1]. Hydroxyapatite (HA,  $Ca_{10}(PO_4)_6(OH)_2$ ) is the most popular ceramic material that belongs to a category of phosphate biomaterials to be used as bone substitutes. HA has been used in a wide variety of biomedical applications because of its biocompatibility as an implant [2, 3]. Numerous types of calcium phosphate (Ca-P) matrices, such as fluorapatite (FA,  $Ca_{10}(PO_4)_6F_2$ ), tricalcium phosphate (TCP,  $Ca_3(PO_4)_2$ ), and HA+ $\beta$ -TCP biphasic calcium phosphate (BCP) in addition to HA are well known because of their wide medical and dental applications [4].

Some ceramic materials are biocompatible and osteoconductive [5, 6]. Other ceramic materials are resorbing and able to stimulate ontogenesis after

degradation takes place. HA is partially degradable and  $\beta$ -TCP is resorbable [7]. Thus, the Ca-P biomaterials are of great interest in bone implants as they show biocompatibility and bioactivity [8]. Concerning the biological applications of the prepared material, it was reported [9] that the BCP is a mixture of non-resorbable HA and the resorbable  $\beta$ -TCP and this has a great probability for bone replacement and bone regeneration.

The bone repair has been widely known using BCP rather than HA alone [9] due to the defects of the non-biodegradable HA material that arise after implantation by implants of calcined HA with high crystallinity [10]. There is an increasing interest in BCP to achieve the formation of material which is consisting of HA with lower biodegradation and  $\beta$ -TCP with higher biodegradation (bio-resorbable). Doping Ca-P matrix with ions such as Ag, Cu, Zn, and Ti improves the properties of the materials e.g. solubility, particle size, electrical-, optical-, dielectric- and antimicrobial properties [11]. In many

\*Corresponding author e-mail: [saraelsayed228@gmail.com](mailto:saraelsayed228@gmail.com); (S. Mohamed).

EJCHEM use only: Received 02 October 2021; revised 09 November 2021; accepted 19 December 2021

DOI: 10.21608/EJCHEM.2021.99125.4612

©2022 National Information and Documentation Center (NIDOC)

glass compositions, metal nanoparticles, e.g. Ag, Au act as volume nucleation agents [12].

Synthetic HA has a crystallographic and chemical composition close to natural bone minerals, however, it is limited by a lower solubility compared with other popular implant materials such as TCP [13]. Different techniques have been used for the synthesis of HA bio-ceramic and Ca-P-based materials, such as hydrothermal [14, 15], solid-state reaction [16], wet chemical reaction [17, 18], or sol-gel methods [19, 20]. The most common methods for the preparation of HA include wet chemical precipitation (aqueous-based solvent) and sol-gel (organic-based solvent) [19]. The degree of agglomeration between nano-sized particles is less in organic solvents than in aqueous-based systems [21].

Temperatures higher than 1000 °C are usually required to obtain apatite crystals prepared by wet precipitation methods, low temperature of the apatite crystals formation is the main step of the sol-gel process as temperatures lower than above are needed to synthesis sol-gel HA [22, 23].

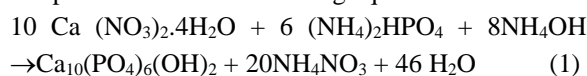
Thus, the current strategy reports the preparation of Ag-doped hydroxyapatite composites by solution method with controlling different conditions. The role of Ag and thermal treatment on the formation and growth of HA,  $\beta$ -TCP, and BCP (HA+ $\beta$ -TCP) were critically assigned.

## 2. Experimental

A series of five Ag-HA samples of the general formula  $[\text{Ca}_{10-x}\text{Ag}_x(\text{PO}_4)_6(\text{OH})_2]$ , was prepared with different Ag contents ( $x = 0, 0.4, 0.8, 1.2,$  and  $1.6$  mole) at constant total content of  $(\text{Ca} + \text{Ag}) / \text{P}$  of 10:6. Ethanol and distilled water were used in the solution as a solvent that gave a relatively viscous solution as a product. Presence of ethanol in  $\text{Ca}(\text{NO}_3)_2 \cdot 4\text{H}_2\text{O}$  and  $(\text{NH}_4)_2\text{HPO}_4$  solutions supported the changes during the formation of calcium

phosphates from the cluster to crystallite forms, and provides a thermally stable HA formation at a lower temperature [24].

The optimized parameters of ammonium hydroxide (pH 9), aging time for 72 h, drying at 80 and 250°C were used in the preparation technique. The addition of Ca- or (Ag + Ca)-containing solution into the P-containing solution leads to a gradual increase of viscosity and formation of white, yellow, and gray colors, depending on the content of Ag [25, 26]. The salts  $\text{Ca}(\text{NO}_3)_2 \cdot 4\text{H}_2\text{O}$  and  $(\text{NH}_4)_2\text{HPO}_4$  were used as Ca and P precursors respectively in the solution method for preparation of the studied samples based on the following equation:



According to the above equation, the formula, Ca/Ag ratio, contents of raw materials in grams, and symbol of the prepared samples are summarized in Table 1.

Differential thermal analysis (DTA) and thermo-gravimetric analysis (TGA) (Perkin Elmer, 7 series Thermal Analysis) were performed on a Perkin Elmer, 7 series Thermal Analysis coupled with a (SDT Q600) using 19 mg of (0.4Ag-HA) composition. The analysis was carried out between 25–1000 °C at a heating rate of 10 °C/min and the output was used to determine the stages of decomposition, the weight loss, and thermal characteristics of the sample.

X-ray diffraction (XRD) of the dried phases and heat-treated compositions was recorded on a Bruker Axs-D8 Advance diffractometer, equipped with a  $\text{CuK}\alpha$  source ( $\lambda = 0.15406 \text{ nm}$ ) in step mode, with intervals of  $0.02^\circ$ , over a  $2\theta$  range of  $4^\circ$ – $70^\circ$  using a dwell time of 0.4 seconds. Phase identification was carried out using X'Pert High Score Plus (PANalytical, Netherlands).

Table 1. The formula, Ca/Ag ratio, contents of raw materials in grams, and symbol of the prepared samples

Formula	Ca/Ag ratio	Contents in grams			Symbol
		$\text{Ca}(\text{NO}_3)_2 \cdot 4\text{H}_2\text{O}$	$\text{AgNO}_3$	$(\text{NH}_4)_2\text{HPO}_4$	
$\text{Ca}_{10}(\text{PO}_4)_6(\text{OH})_2$	10/0	11.80	0	3.96	0 Ag-HA
$\text{Ca}_{9.6}\text{Ag}_{0.4}(\text{PO}_4)_6(\text{OH})_2$	9.6/0.4	11.33	0.33	3.96	0.4 Ag-HA
$\text{Ca}_{9.2}\text{Ag}_{0.8}(\text{PO}_4)_6(\text{OH})_2$	9.2/0.8	10.80	0.67	3.96	0.8 Ag-HA
$\text{Ca}_{8.8}\text{Ag}_{1.2}(\text{PO}_4)_6(\text{OH})_2$	8.8/1.2	10.39	1.01	3.96	1.2 Ag-HA
$\text{Ca}_{8.4}\text{Ag}_{1.6}(\text{PO}_4)_6(\text{OH})_2$	8.4/1.6	9.91	1.35	3.96	1.6 Ag-HA

The FTIR spectra of the studied samples were recorded on A Mattson 5000 FTIR spectrometer in the range between 400 and 2000  $\text{cm}^{-1}$  with a resolution of 2  $\text{cm}^{-1}$  at room temperature using the KBr disk technique. For this measurement, the studied samples were ground to a fine powder and mixed with KBr at a ratio of 1:100 in weight. The spectrum of each sample is an average of 30 scans.

The morphology of the prepared samples was studied using a JEOL JSM-6510 LV scanning electron microscope (SEM) operated at accelerating voltage 30 kV, with a magnification 10 X up to 400.000 X. For the SEM study, the samples were coated with gold to prevent scattering of the electron beam. The elements present in the sample were obtained by an energy dispersive X-Ray analyzer (EDS) coupled with SEM.

Transmission electron microscope (TEM) and electron diffraction pattern (EDP) were used to explore the morphology of the particles and phase identification. Electron micrographs were obtained using a JEOL JEM-2100 Electron Microscope. For this, samples were suspended in ethanol using MCS Digital Ultrasonic Heater. The samples were loaded on a grid and let to dry and are then inserted into the instrument and examined.

### 3. Results and discussion

#### 3.1. Thermal Analysis

To evaluate the thermal properties of the samples, TGA and DSC thermal analyses were performed on 0.4 Ag-HA composite (Figure 1. a, b) from room temperature to 1000 °C. The evaporation of absorbed water and the thermal decomposition of the solvent molecules, linkers, and the pure product can be attributed to the weight loss observed between 35 °C - 500 °C, according to TGA for the composite (Fig.1 -a) [27-30]. TGA further revealed that the weight of the 0.4 Ag-HA composite was reduced in three phases, with the pure product being obtained at around 250 °C, which agrees well with that reported by Sargazi et al. [27] on electrospun composite containing Ta-MOF and PVA nanofibrous.

At approximately 60 °C (mass change: 11%), the adsorbed water evaporated, resulting in the first weight loss step. This event might lead to leaving behind pure 0.4 Ag-HA [28]. Between 60 °C and 260 °C, the major weight loss is assigned to the decomposition and the evaporation of ammonia [28, 31]. Dehydration of 0.4 Ag-HA also contributes to a part of this weight loss and the total weight loss in

this second stage is found to be ~ 42% (mass change: 42%). The third stage is a weight loss that occurs between 260 °C and 480 °C. This loss is due to the decomposition of nitrate [32]. The total weight loss is found to be ~ 61%. Thermo-gravimetric analysis indicates that between 500 °C and 1000 °C there is no significant weight loss and the residual components of the composites were disintegrated [28]. An almost stable curve was noticed within this temperature range, which indicates good thermal stability of HA powder and this agrees well with that previously reported by Anee et al. [33].

The temperatures linked with the highest rate of weight loss in each step are shown as derivative (DSC) peaks, Fig.1 -b. The DSC peaks match the endothermic peaks, indicating that all of the thermal events seen are due to weight loss without any considerable phase change for the sample under the studied temperature range, there was no significant phase change for the sample such behavior agrees well with that previously reported by Sargazi et al. [34].

Three endothermic peaks (60°C, 244°C, and 490°C) are displayed in the DTA curve of 0.4 Ag-HA (Fig. 1 b). These endothermic peaks recommend the selected range of the temperature of heat treatment in order to study the effect of heat treatment on the studied composites containing different Ag contents. At low temperatures, the observed small endothermic peaks revealed that lower energy is required to form crystalline apatite from the amorphous Ca-P intermediate [26]. Based on TGA and DTA analyses, the heat treatment of the prepared samples was performed at 700 °C, 800 °C, 900 °C, and 1000 °C for 1h and 4 hours.

#### 3.2. XRD characterization

The XRD patterns of the prepared and heat-treated Ag-HA ( $\text{Ca}_{10-x}\text{Ag}_x(\text{PO}_4)_6(\text{OH})_2$ , where  $x = 0, 0.4, 0.8, 1.2, \text{ and } 1.6$  mole) samples are illustrated in Figures. 2-4. Obvious changes in the patterns were noticed due to the change in temperature, time of heat treatment, and Ag content. The phases identified are HA phase [JCPDS File No. 76-0694],  $\beta$ -TCP phase [JCPDS File No. 09-0169], metallic Ag phase [JCPDS File No. 01-1167],  $\text{Ag}_3\text{O}_4$  phase [JCPDS File No. 40-1054], and  $\text{Ag}_3\text{PO}_4$  phase [JCPDS File No. 70-0702]. Mono phase  $\beta$ -TCP is obtained at as prepared condition see (Fig. 2). With Ag substitution, the obtained phases are  $\beta$ -TCP and Ag-related phase

(Ag<sub>3</sub>O<sub>4</sub>) (Fig. 2) where the characteristic peaks of the latter phase appeared at  $2\theta \sim 26^\circ$ ,  $34^\circ$ , and  $41^\circ$ .

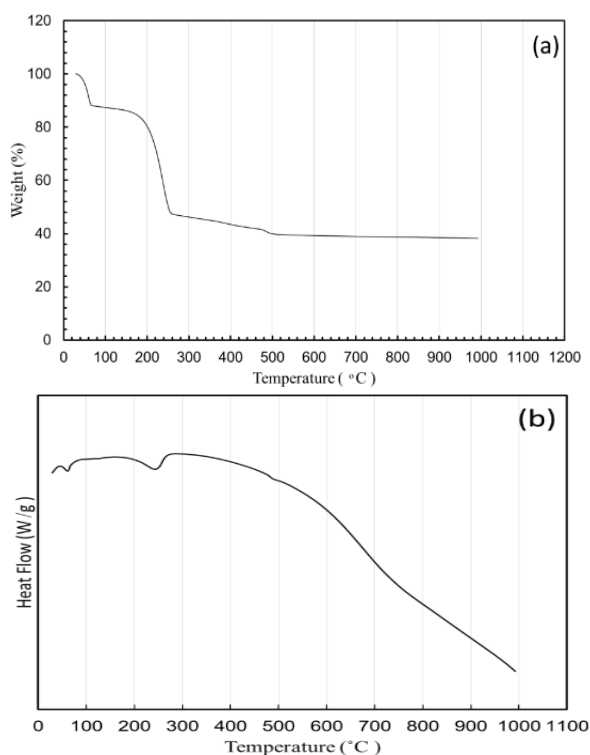


Fig. 1: Thermal analysis results; (a) TGA and, (b) DTA curves of 0.4 Ag-HA composition.

The color changes of the studied composites are also interesting. The undoped composites remained constantly white, while the doped composites were yellow at the as-prepared condition (pale yellow for the 0.4 and 1.2 and yellow for the 0.8 and 1.6), then turned to grey, brown, and some composites are bleached up to 700 °C, 800 °C, 900 °C, and 1000 °C. The grey color can be attributed to the Ag nanoparticles [29] present in the Ag-CaPs composites, these colors deal with the phases that are obtained from XRD patterns. It is therefore normal to lose the grey color above 1000 °C since Ag has a melting point of 962 °C as previously discussed [29]. Although in this study as an example, the white color appears at approximately 800 °C for 1h for 0.8 Ag-CaP bio composite.

The XRD pattern of the first step of heat treatment applied at 700 °C (1h) on undoped sample (Fig. 3-a) shows that the crystalline phase is presented as  $\beta$ -TCP with HA peak at  $2\theta \sim 32^\circ$ . In XRD patterns, Ag substitution also results in different crystalline phases such as a mixture of crystalline (HA+ $\beta$ -TCP) and metallic Ag phase. Also, metallic Ag phase can be observed at  $2\theta \sim 38^\circ$  and  $45^\circ$ . It is

clear that additions of Ag activate the formation of (HA+ $\beta$ -TCP) phases. Owing to these results, Ag may be considered to play as a nucleating agent in the matrix, which agrees with previously reported [12, 35].

Increasing the time of heat treatment to 4h, (Fig. 3-b) supports the formation of HA instead of (HA+ $\beta$ -TCP) in the samples with zero Ag content. Doping by Ag results in the formation of the  $\beta$ -TCP phase in addition to the formed HA.

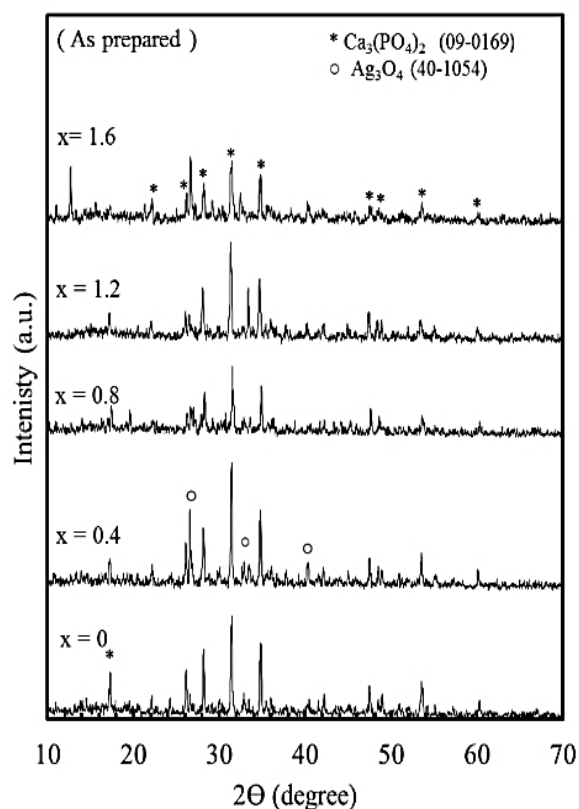


Fig.2: XRD patterns of as-prepared  $\text{Ca}_{10-x}\text{Ag}_x(\text{PO}_4)_6(\text{OH})_2$  compositions.

So, two characteristic phases (HA and  $\beta$ -TCP) in heat treated samples at 700 °C for 4h are formed. Also, a slightly lower intensity of HA peak at  $2\theta \sim 32^\circ$  and the presence of a  $\beta$ -TCP peak at  $2\theta \sim 31^\circ$  with no Ag-phases can be observed for  $x=0.4$ . Reversely, at high Ag content 0.8, 1.2, and 1.6 Ag-HA the main phases may be  $\beta$ -TCP and HA besides metallic Ag and Ag<sub>3</sub>PO<sub>4</sub> phases. The peaks in Fig. 3-b indicate that the thermal energy is insufficient to form new phases at time 4h for samples with low Ag content, whereas the XRD patterns reveal that the compositions 1.2 and 1.6 Ag-HA are rich with phases.

Figure 4 shows XRD patterns of composites treated thermally at 1000 °C for the same times (1 and 4 hours). It is noticed that there is a hump with characteristic crystalline peaks of HA and  $\beta$ -TCP phases. XRD patterns of heat treatment at 1000 °C/1h describe the glass-ceramic nature of the compositions especially with Ag doping which confirms the effect of Ag on the phase formation (Fig. 4-a). It seems that the heat treatment at 1000°C/1h supplies the samples with quite enough thermal energy to establish the glass-ceramic phase. So, the full-crystalline phases

tend to be dissolved at 1000 °C for short time (1 h). In addition, increasing the time of heat treatment from 1h to 4h initiates the formation of polycrystalline phases (Fig. 4-b).

There is good matching between XRD patterns of 1000 °C/ (1, 4h) and each of 800 °C/ (1, 4h) and 900 °C/ (1, 4h). Phases obtained from XRD patterns of compositions treated thermally at 700 °C, 800 °C, 900 °C, and 1000 °C for the same intervals (1 and 4 hours) are summarized in **Table 2**.

Table 2. The phases obtained from XRD patterns as a function of temperature, time, and silver content

Conditions Composition	0 Ag-HA	0.4 Ag-HA	0.8 Ag-HA	1.2 Ag-HA	1.6 Ag-HA
As-prepared	Crystalline $\beta$ -TCP	Crystalline $\beta$ -TCP+Ag <sub>3</sub> O <sub>4</sub>	Crystalline $\beta$ -TCP+Ag <sub>3</sub> O <sub>4</sub>	Crystalline $\beta$ -TCP+Ag <sub>3</sub> O <sub>4</sub>	Crystalline $\beta$ -TCP+Ag <sub>3</sub> O <sub>4</sub>
(700 °C for 1h)	Crystalline HA+ $\beta$ -TCP	Crystalline $\beta$ -TCP +Ag	Crystalline HA+ $\beta$ -TCP +Ag	Crystalline $\beta$ -TCP+Ag	Crystalline HA + $\beta$ -TCP+Ag
(700 °C for 4h)	Crystalline HA	Crystalline HA + $\beta$ -TCP	Crystalline HA+ $\beta$ -TCP +Ag	Crystalline HA + $\beta$ -TCP +Ag	Crystalline HA+ $\beta$ -TCP +Ag +Ag <sub>3</sub> PO <sub>4</sub>
(800 °C for 1h)	Crystalline HA+ $\beta$ -TCP	Glass-ceramic HA+ $\beta$ -TCP	Glass-ceramic HA+ $\beta$ -TCP +Ag	Glass-ceramic $\beta$ -TCP	Glass-ceramic $\beta$ -TCP+Ag <sub>3</sub> O <sub>4</sub>
(800 °C for 4h)	Crystalline HA+ $\beta$ -TCP	Crystalline HA+ $\beta$ -TCP +Ag	Crystalline $\beta$ -TCP +Ag	Crystalline HA+ $\beta$ -TCP +Ag	Crystalline HA + $\beta$ -TCP+ Ag <sub>3</sub> PO <sub>4</sub>
(900 °C for 1h)	Glass-ceramic $\beta$ -TCP	Glass-ceramic HA + $\beta$ -TCP	Glass-ceramic HA + $\beta$ -TCP	Glass-ceramic $\beta$ -TCP +Ag <sub>3</sub> PO <sub>4</sub>	Glass-ceramic $\beta$ -TCP +Ag <sub>3</sub> O <sub>4</sub>
(900 °C for 4h)	Crystalline HA+ $\beta$ -TCP	Crystalline HA+ $\beta$ -TCP +Ag	Crystalline $\beta$ -TCP+Ag	Crystalline HA+ $\beta$ -TCP +Ag	Crystalline $\beta$ -TCP
(1000 °C for 1h)	Glass-ceramic HA + $\beta$ -TCP	Glass-ceramic HA + $\beta$ -TCP	Glass-ceramic $\beta$ -TCP +Ag	Glass-ceramic HA+ $\beta$ -TCP +Ag	Glass-ceramic $\beta$ -TCP+Ag <sub>3</sub> O <sub>4</sub>
(1000 °C for 4h)	Crystalline HA+ $\beta$ -TCP	Crystalline HA+ $\beta$ -TCP	Crystalline $\beta$ -TCP +Ag	Crystalline $\beta$ -TCP+ Ag <sub>3</sub> PO <sub>4</sub>	Crystalline HA + $\beta$ -TCP+Ag

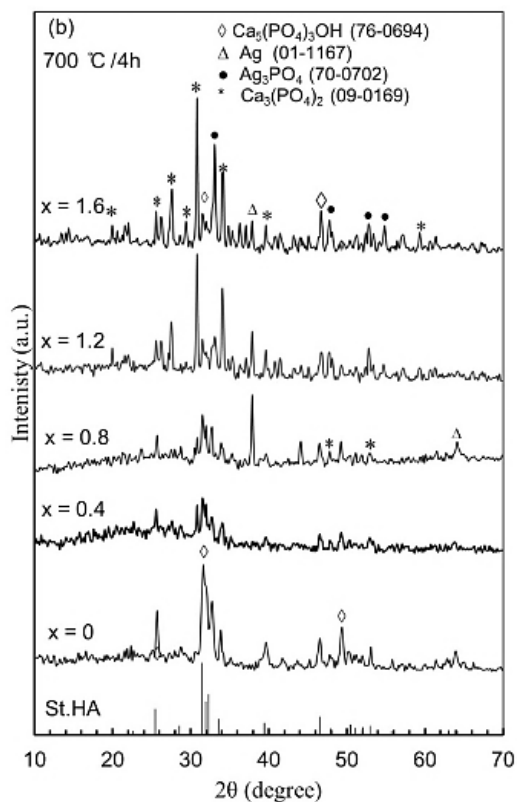
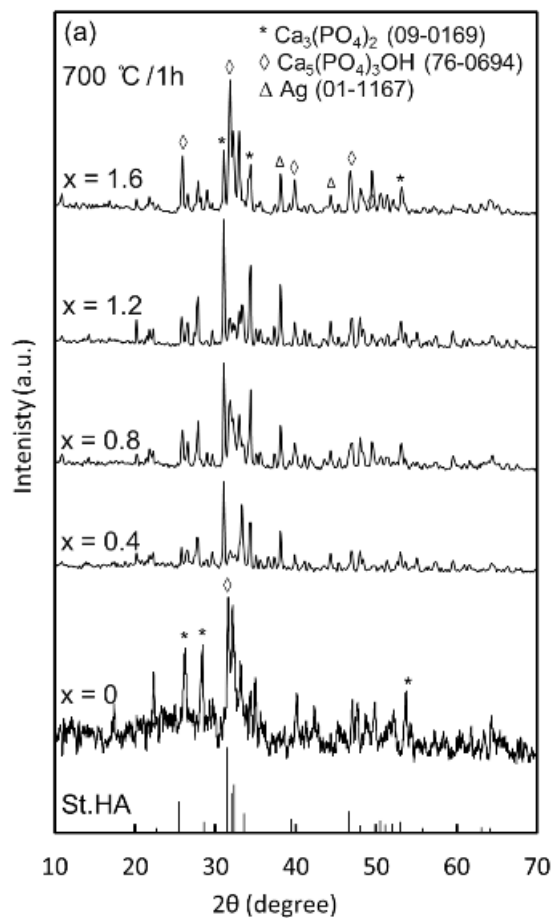


Fig. 3: XRD patterns of  $\text{Ca}_{10-x}\text{Ag}_x(\text{PO}_4)_6(\text{OH})_2$  compositions; (a) H.T. at 700 °C for 1h, and (b) H.T. at 700 °C for 4h.

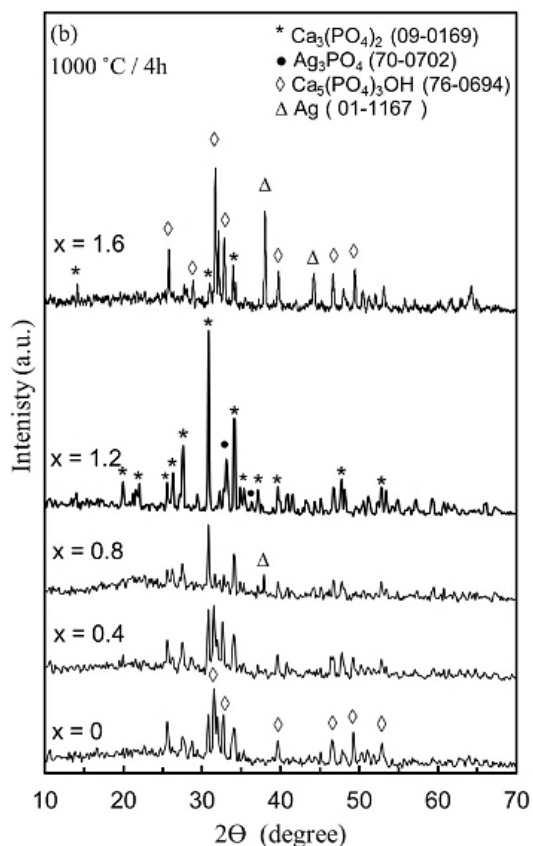
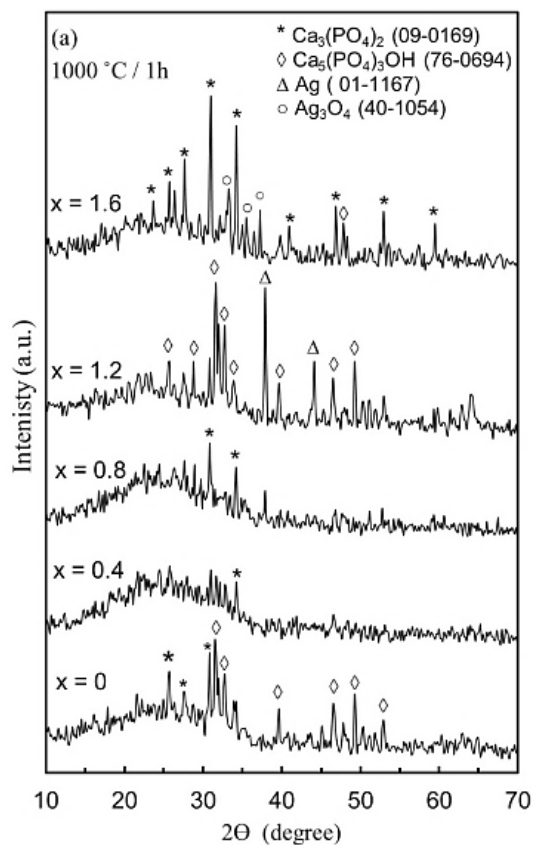


Fig. 4: XRD patterns of  $\text{Ca}_{10-x}\text{Ag}_x(\text{PO}_4)_6(\text{OH})_2$  compositions; (a) H.T. at 1000 °C for 1h and (b) for 4h.

From the XRD results, it can be concluded that heat treatment is necessary to form HA and/or  $\beta$ -TCP phases. At the lower time, raising the temperature tends to transform the crystalline phase to the glass-ceramic and Ag doping with different concentrations tends to form HA,  $\beta$ -TCP, BCP (HA+ $\beta$ -TCP), and other phases that belong to Ag ion. Thus, XRD results indicate that each of HA and  $\beta$ -TCP, as phases for bio-applications, have been successfully synthesized using the solution method. The metallic Ag and Ag phases obtained from XRD patterns seem to activate the formation of Ag-HA compositions. This agrees well with a lot of recent research on the characteristics of HA that has been studied [36-40], although these characteristics are still not very clear.

Partial decomposition of HA into tricalcium phosphate was also reported by Raynaud et al. [41]. This decomposition was also observed when the HA was heat treated at 900 °C and 1000 °C and/or with Ag doping at lower temperatures 700 °C and 800 °C. The Degree of crystallization (DOC) has been calculated by dividing the integrated intensity of XRD patterns, using the material studio program. DOC was found to be 50-65% for samples heat-treated at 700 °C for 1h and 49-64% for 700 °C/4h which indicates the increase of crystallinity with increasing Ag concentration and the heat treatment process. Moreover, it was 18-55% for 800 °C/1h and 50-69% for 800 °C/4h reflecting the decrease of crystallinity with increasing Ag concentration. The value of the degree of crystallinity was 39-57% for 900 °C/1h and 51-68% for 900 °C/4h. The degree of crystallinity was found to be 45-58% for HA heat-treated at 1000 °C for 1h and increases to 57-73% for that heat treated at 1000 °C for 4h.

The results of HA's dissolution properties are also significantly influenced by crystallinity. Okazaki et al. [42, 43] reported that carbonated-apatite and fluoridated-HA solubility increased with increasing ionic substitutions and decreasing crystallinity in the apatite lattice. Fulmer et al. [44] had concluded that

sintered HA, being well crystallized, has a far lower solubility than poorly crystallized biological HA. The crystallinity of Ag-HA shows an increase with Ag doping. The decrease of the crystallinity at low Ag content may be due to the interference of Ag ions with the crystal growth [38].

The results show that Ag atoms may be found in three different places in the produced composites, as well as two different chemical states (metallic and ionic). A portion of the inserted Ag cations is detected in the metallic state, in the form of nanoparticles and this agrees well with that reported before by Jacobs et al. [29]. The rest is in the cationic form, either in the HA,  $\beta$ -TCP, or BCP phases as seen (at low temperatures: 700 °C) for the 0.4 Ag-BCP composite sintered at 700 °C /4h. And as an example, (at higher temperatures: up to 1000 °C) in the 1.6 Ag- $\beta$ -TCP composite sintered at 1000 °C /1h, these results agree well with that discussed by Jacobs et al. [29].

Crystallinity gradually decreased in intensity when the sample is heated from 700 °C up to 800 °C, 900 °C, and 1000 °C/1 h holding time at each temperature in agreement with the XRD results.

### 3.3. FTIR Spectra

The FTIR spectra of the prepared and sintered composites with and without different contents of Ag are displayed in Figs. 5-7. The main features of FTIR spectra of the studied samples are the presence of two basic absorption envelopes in the region 900-1200  $\text{cm}^{-1}$  and 500-700  $\text{cm}^{-1}$  were noticed. The absorption peaks were also splatted into two or three distinct peaks in addition to other absorption bands at 420-450  $\text{cm}^{-1}$ , 820 and 1380  $\text{cm}^{-1}$ , 715 and 960  $\text{cm}^{-1}$ , 975 and 1100  $\text{cm}^{-1}$ . The different FTIR bands and their assignments are summarized in **Table 3**.

Absorption of the envelope between 900 and 1200  $\text{cm}^{-1}$  is attributed to symmetric ( $\nu_1$ ) and asymmetric ( $\nu_3$ ) P-O stretching modes of  $\beta$ -TCP and HA phosphate groups [44].

**Table 3. FTIR spectral data of the studied samples and their tentative assignments**

Wavenumber ( $\text{cm}^{-1}$ )	Assignments	References
960, 975 and 1100	$\beta$ -TCP shoulders	[42]
715	$\text{P}_2\text{O}_7^{4-}$	[42]
500-603	$\text{PO}_4^{3-}$ bending mode	[42]
630	OH liberational mode	[43]
820 and 1380	$\text{NO}_3^-$ or $\text{CO}_3^{2-}$	[37,43,44]
1032 and 1094	$\text{PO}_4^{3-}$ stretching mode	[42]

Generally, the form of the  $\nu_1$ ,  $\nu_3$  absorbance 900-1200  $\text{cm}^{-1}$  is changed in some cases from an overlapping narrower band to broader ones, which generally featureless (except for the shoulder at 960  $\text{cm}^{-1}$  and 1100  $\text{cm}^{-1}$ ) seen in ACP (Amorphous calcium phosphate) and  $\beta$ -TCP [45]. Also, the broad  $\nu_4$  absorbance band in the 500-700  $\text{cm}^{-1}$  region refers to the asymmetric P-O bending modes of the phosphate groups ( $\text{PO}_4^{3-}$ ) which is resolved into two distinct peaks or three that are characteristics of HA [46].

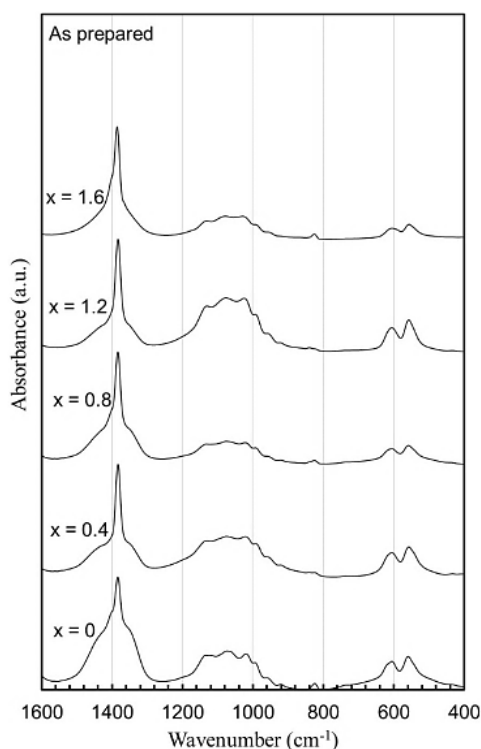


Fig. 5: Normalized FTIR spectra of  $\text{Ca}_{10-x}\text{Ag}_x(\text{PO}_4)_6(\text{OH})_2$  samples.

At the FTIR analysis, mainly the peaks of  $\text{PO}_4^{3-}$  and  $\text{OH}^-$  groups in HA are noticed. Peaks at 560-610  $\text{cm}^{-1}$  and 1000-1100  $\text{cm}^{-1}$  must be due to  $\text{PO}_4^{3-}$ . For  $\text{OH}^-$  group the peak position is nearly at 630  $\text{cm}^{-1}$  that appears at the triplet peak of  $\nu_4$  band. The special bands related to  $\text{NO}_3^-$  or  $\text{CO}_3^{2-}$  groups are at 820 and 1380  $\text{cm}^{-1}$ , while that of  $\text{P}_2\text{O}_7^{4-}$  was located at 715  $\text{cm}^{-1}$  and these of  $\beta$ -TCP are at 960, 975 and 1100  $\text{cm}^{-1}$  and this agree well with that reported previously [40,45-48]. It was noted that it is possible to determine which type of apatite, poorly or well-crystallized, is formed. The contour in the 900-1200  $\text{cm}^{-1}$  spectral region is much narrower for the well-crystallized apatite's and the  $\nu_1$  at (950-970)  $\text{cm}^{-1}$  was resolved [44]. Pleshko et. al [45] described a novel

method of IR to test the HA mineral crystallinity, based on the changes in the 900-1200  $\text{cm}^{-1}$  phosphate  $\nu_1$  and  $\nu_3$  absorbance spectral region. An IR process was developed by Termine and Posner (1966) to determine the percentage of apatite crystallinity minerals, based on the phosphate  $\nu_4$  mode changes [49].

The peaks at approximately 1380  $\text{cm}^{-1}$  and 817  $\text{cm}^{-1}$  (Fig.5) of the prepared samples are most likely related to  $\text{NO}_3^-$ . The region between 900-1200  $\text{cm}^{-1}$  and the duplet bands at 500-700  $\text{cm}^{-1}$  have small area under the bands which increases as the heat treatment process takes place as will be seen in Figs. 6-7. These figures show that the IR spectra of the calcium phosphate precipitates treated at different temperatures for different time intervals are significantly altered as the Ag-HA crystals combined with  $\beta$ -TCP mature.

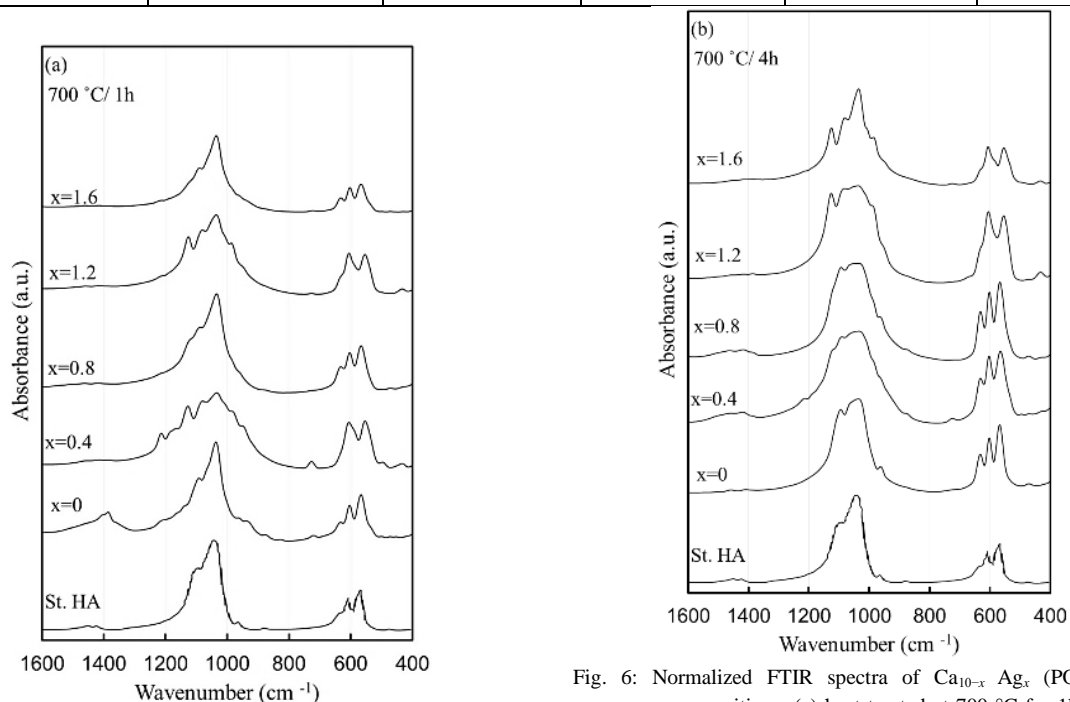
The first step of heat treatment is 700  $^\circ\text{C}/1\text{h}$  [Fig. 6-a] presents the intensity of the  $\nu_1$ ,  $\nu_3$ , and  $\nu_4$  absorbance progressively increases compared with as-prepared conditions. For  $x=0$ , the shape of the  $\nu_1$  and  $\nu_3$  absorbance is a composite of narrower overlapping bands from which a high-frequency shoulder at  $\sim 1100$   $\text{cm}^{-1}$  ( $\beta$ -TCP) gradually emerges. The band at  $\sim 1380$   $\text{cm}^{-1}$  is related to  $\text{CO}_3^{2-}$  [40,46,47] and reflects the formation of carbonated (HA+ $\beta$ -TCP). The higher content of Ag does not change the above features. It is observed that the set of these samples presents a greater intensity in the 630  $\text{cm}^{-1}$  band, corresponding to the hydroxyl functional group  $\text{OH}^-$  [46].

The set of  $x=0.4$  and  $x=1.2$  exhibits an increase in the phosphate groups (900-1200)  $\text{cm}^{-1}$  with two shoulders at 1100  $\text{cm}^{-1}$  and 960  $\text{cm}^{-1}$  which are related to  $\beta$ -TCP [46]. And the band belonging to  $\text{OH}^-$  at 630  $\text{cm}^{-1}$  is lower in these instances or does not appear. The presence of  $\text{OH}^-$  reflects the HA formation [46], the absence of  $\text{OH}^-$  and the presence of  $\beta$ -TCP shoulder means the partial or complete decomposition of HA and the growth of  $\beta$ -TCP phase in the matrix. Fig. 6-b presents FTIR spectra when raising the time of heat treatment to 4h which show the same spectral features.

Raising the heat treatment temperature to 1000  $^\circ\text{C}$  for 1h and 4h is presented in [Fig.7 a, b]. Phases obtained from FTIR spectra according to the above-mentioned assignments of compositions treated thermally at 700  $^\circ\text{C}$ , 800  $^\circ\text{C}$ , 900  $^\circ\text{C}$ , and 1000  $^\circ\text{C}$  for the same intervals (1 and 4 hours) are given in **Table 4**.

**Table 4. Impact of temperature, time, and silver content changes on the formed phases based on FTIR spectra**

Conditions / Composition	0 Ag-HA	0.4 Ag-HA	0.8 Ag-HA	1.2 Ag-HA	1.6 Ag-HA
As-prepared	Crystalline $\beta$ -TCP	Crystalline $\beta$ -TCP	Crystalline $\beta$ -TCP	Crystalline $\beta$ -TCP	Crystalline $\beta$ -TCP
(700 °C for 1h)	Crystalline carbonated (HA+ $\beta$ -TCP)	Crystalline $\beta$ -TCP	Crystalline HA + $\beta$ -TCP	Crystalline $\beta$ -TCP	Crystalline HA + $\beta$ -TCP
(700 °C for 4h)	Crystalline HA + $\beta$ -TCP	Crystalline HA + $\beta$ -TCP	Crystalline HA + $\beta$ -TCP	Crystalline $\beta$ -TCP	Crystalline $\beta$ -TCP
(800 °C for 1h)	Crystalline HA + $\beta$ -TCP	Poorly-crystalline HA + $\beta$ -TCP	Poorly-crystalline HA + $\beta$ -TCP	Poorly-crystalline $\beta$ -TCP	Poorly-crystalline $\beta$ -TCP
(800 °C for 4h)	Crystalline HA+ $\beta$ -TCP	Crystalline HA + $\beta$ -TCP	Crystalline HA+ $\beta$ -TCP	Crystalline HA + $\beta$ -TCP	Crystalline HA+ $\beta$ -TCP
(900 °C for 1h)	Poorly-crystalline carbonated $\beta$ -TCP	Poorly-crystalline carbonated (HA + $\beta$ -TCP)	Poorly-crystalline carbonated (HA + $\beta$ -TCP)	Poorly-crystalline carbonated $\beta$ -TCP	Poorly-crystalline carbonated $\beta$ -TCP
(900 °C for 4h)	Crystalline HA+ $\beta$ -TCP	Crystalline HA + $\beta$ -TCP	Crystalline $\beta$ -TCP	Crystalline HA + $\beta$ -TCP	Crystalline $\beta$ -TCP
(1000 °C for 1h)	Poorly-crystalline HA + $\beta$ -TCP	Poorly-crystalline HA + $\beta$ -TCP	Poorly-crystalline $\beta$ -TCP	Poorly-crystalline HA + $\beta$ -TCP	Poorly-crystalline $\beta$ -TCP
(1000 °C for 4h)	Crystalline $\beta$ -TCP	Crystalline $\beta$ -TCP	Crystalline $\beta$ -TCP	Crystalline $\beta$ -TCP	Crystalline HA + $\beta$ -TCP

Fig. 6: Normalized FTIR spectra of  $\text{Ca}_{10-x}\text{Ag}_x(\text{PO}_4)_6(\text{OH})_2$  compositions, (a) heat-treated at 700 °C for 1h and (b) heat-treated at 700 °C for 4h.

FTIR spectral data revealed the characteristic absorption peaks of HA and  $\beta$ -TCP in the prepared samples. The heat treatment process has revealed a huge influence on the formation of HA and  $\beta$ -TCP as the phosphate groups of  $\nu_1$ ,  $\nu_3$ , and  $\nu_4$  spectral regions mature and OH<sup>-</sup> shoulder and support the partial decomposition of HA into tricalcium phosphate [37-40]. Ag doping with different concentrations does not change the functional groups, however, it has the role besides heat treatment and time interval to control each of, HA partial decomposition into  $\beta$ -TCP, growth of HA from  $\beta$ -TCP, and the degree of crystallinity of HA and/or  $\beta$ -TCP.

### 3.4. Analysis of SEM, EDS, TEM and EDP data

The morphology of the sample's matrices of the prepared samples is studied by SEM, EDS, TEM, and EDP. The SEM graphs for 0 and 0.8 Ag-HA, as examples, are shown in Fig. 8 (a, b). It was found that from Fig. 8-a for HA free from Ag, the sample consists of rods-like structure, that is matched in shape with the structure of HA reported elsewhere [50]. However, the addition of Ag content in the sample (0.8 Ag-HA) causes an apparent change in the morphology of the obtained sample. On the other hand, Fig. 8-b shows non-uniform distribution of agglomerates and particles on the surface. These results can be interpreted as an effect of the formation of HA and  $\beta$ -TCP in addition to Ag phases.

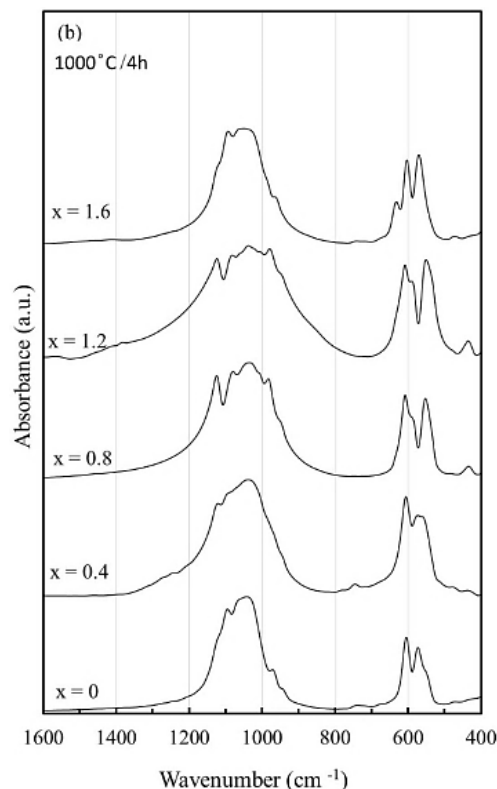
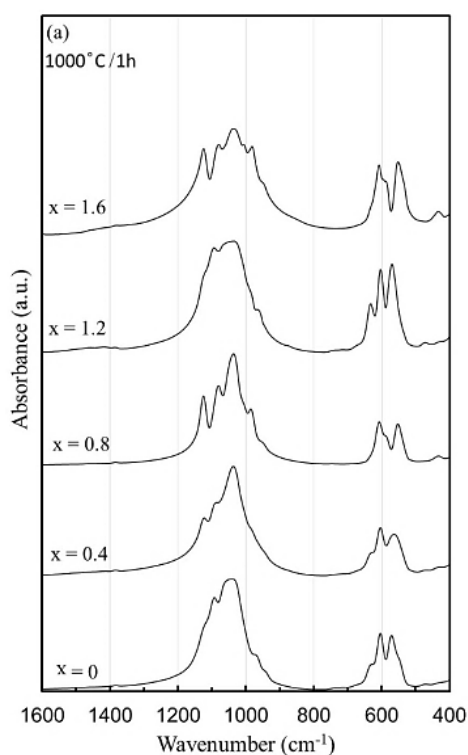


Fig. 7: Normalized FT-IR spectra of  $\text{Ca}_{10-x}\text{Ag}_x(\text{PO}_4)_6(\text{OH})_2$  compositions, H.T. at 1000 °C for 1h (a) and for 4h (b).

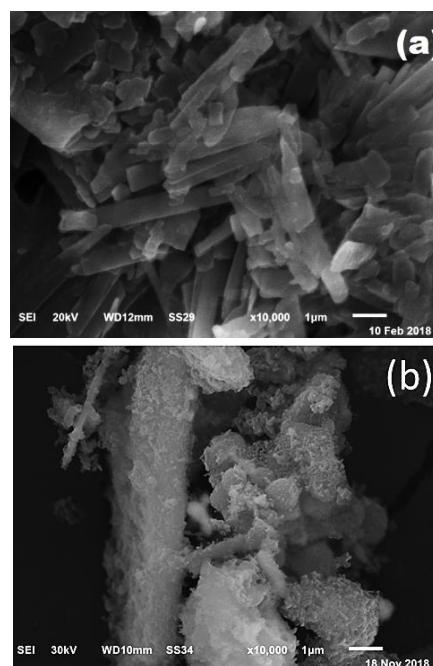


Fig. 8: SEM micrographs of (a) 0 mole% and (b) 0.8 mole% Ag-HA, H.T. at 700 °C for 1h.

Ca/P ratio of undoped HA and doped HA, heat-treated at 700 °C/1h, was estimated by EDS analysis [Fig. 9 (a, b)]. The EDS spectrum [Fig. 9-a] of 0 Ag-HA sample confirms the presence of calcium (Ca), phosphor (P), and oxygen (O) atoms. Its Ca/P ratio

was found to be 1.60 which is between 1.67 of standard HA and 1.5 of  $\beta$ -TCP [51]. This ratio is in good agreement with the expected stoichiometric HA based on the chemical structure of HA (1.67; Ishikawa et al. 1993). Whereas, the Ag-HA with 0.8 of Ag is composed of Ca, P, O, and Ag as shown in [Fig.9-b] presenting the Ca/P ratio equals 1.29. The addition of Ag causes the decrease of the Ca/P ratio from 1.60 to 1.29. These results present the transform of stoichiometric HA to non-stoichiometric HA ( $\beta$ -TCP) [52]. As revealed by the XRD analysis, the obtained phase is transformed from (HA+ $\beta$ -TCP) to metallic Ag that was found in 0.8 Ag-HA composition besides the formation of  $\beta$ -TCP with high intensity. From the SEM micrographs and EDS spectrum, the different phases formed in the studied samples are affected by the role of Ag as a nucleating agent, and such results are confirmed by the morphology of the formed phase and its Ca/P ratio.

**Table 5** presents the morphology and phase analysis “TEM and EDP images” of HA and HA doped with Ag and heat-treated at different temperatures for different times ( $x=0$  and 0.8 Ag-HA (700 °C, 1h),  $x=0$  (700 °C, 4h),  $x=0$  (900°C, 1h), and  $x=0.8$  (1000 °C, 1h).

TEM morphology of the 0 Ag-HA composition in heat treatment condition at 900 °C for 1h is shown in Fig. 10-a, b, c, d. Fig. 10-a shows that the particles are found to be of nanosized particles with a bit deformed rod-like morphology in range of (45-115) nm. [Fig. 10-b] EDP for dark regions of composite  $x=0$  shows rings having weak diffuse halo with bright spots. According to XRD and EDP results, such an electron diffraction pattern supports the growth of  $\beta$ -TCP on an amorphous matrix.

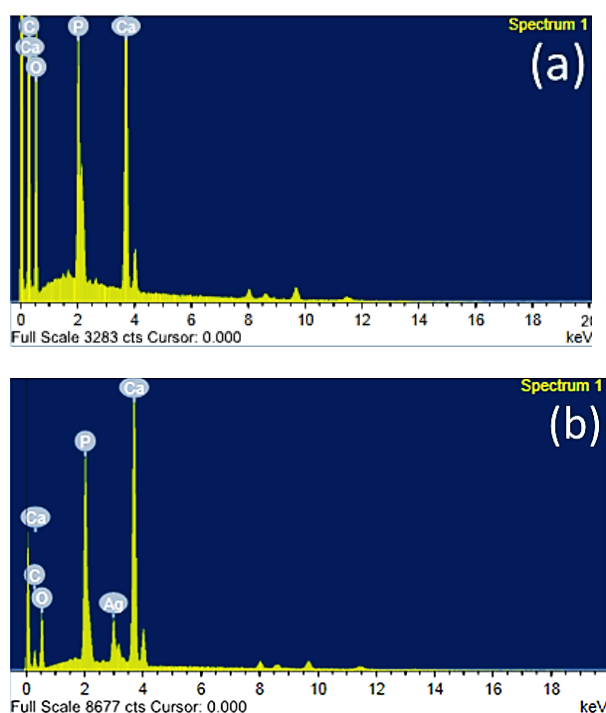


Fig. 9: EDS spectrum of (a) 0 mole% and (b) 0.8 mole% Ag-HA compositions, heat treated at 700 °C for 1h.

[Fig.10-c] shows less clear morphology for the same sample. EDP data in Fig. 10-d reveals that the crystalline phases are dispersed in an amorphous matrix. The pattern consists of spots superimposed with rings belonging to the planes of  $\beta$ -TCP crystal [52]. These particles are assumed to contain a large portion of the glass-ceramic  $\beta$ -TCP phase according to XRD analysis. The TEM/EDP analyses data depending on Ag content, heat treatment time, and temperature are summarized in **Table 5**.

Table 5. Analysis of TEM/EDP data

Composition (Ag-HA)	Thermal Degree (°C)	Treatment Duration (h)	Range of Particle size (nm)	Morphology	Phase
0	700	1	19–27	Rod	HA
0	700	4	29–53	Sphere	HA
0	900	1	45-115	bit deformed rod	$\beta$ -TCP
0.8	700	1	(37-57) in width, (139-259) in length, (34-45) in diameter	Rod and Sphere	HA + $\beta$ -TCP
0.8	1000	1	13-17	Rod and Sphere	$\beta$ -TCP + Metallic Ag

0 Ag-HA H.T.at 900 °C (1h)

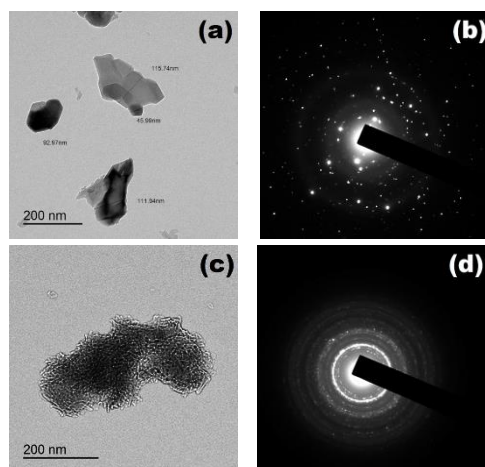


Fig. 10: TEM and EDP images of 0 Ag-HA composite heat treated at 900 °C/1h (a, b, c, d).

Finally, based on the specific features of the prepared HA and its derivatives as Ag-HA,  $\beta$ -TCP, and BCP, such materials are good candidate for different biological applications had been discussed previously by some authors to be used as implants for bone regeneration [5], bone scaffolds [7], tissue engineering [9], bone defects [10], and as bactericidal biomaterial [11].

Kumar et al. reported the development of Ag-Au-HA nanoparticles and they concluded the highly effective properties of these nanoparticles in promoting the bone regeneration in a Zebrafish (ZF) jawbone regeneration model [53].

#### 4. Conclusions

The current study reports a successful preparation of Ag-HA,  $\beta$ -TCP, and BCP nanoparticles with high dispersibility and stability by solution method. Temperature and the time of heat treatment control the phase formation and its crystallinity. Crystalline, polycrystalline, and glass-ceramic phases are obtained at different temperatures. XRD indicates the growth of  $\beta$ -TCP glass-ceramic containing HA ceramic phase at high temperatures for low times. Ag ion as a nucleating agent causes the acceleration of nucleation for HA,  $\beta$ -TCP, and BCP formation. Ca/P molar ratio equal to 1.60 and 1.29 with Ag doping. FTIR results contain the functional groups of HA as  $\text{PO}_4^{3-}$  and OH. The absence of the OH group in FTIR reflects the partial or complete decomposition of HA and the formation of  $\beta$ -TCP. The crystallinity of FTIR spectra is related to the features of  $\nu_1$ ,  $\nu_3$ , and  $\nu_4$  bands. TEM micrographs of the pure samples differ by Ag doping which influences the structure and the size of particles. EDP results show the presence of the polycrystalline and amorphous phases in the matrices. HA,  $\beta$ -TCP, and BCP bio composites

can be used in the biomedical applications to treat bone defects and for bone regeneration.

#### 5. Conflicts of interest

“There are no conflicts to declare”.

#### 6. References

- [1] Blackwood, D.J., Biomaterials: past successes and future problems, *Corrosion reviews*, 21(2-3), pp.97-124 (2003).
- [2] Gross, K.A. and Berndt, C.C., Biomedical application of apatites. *Reviews in mineralogy and geochemistry*, 48(1), pp.631-672 (2002).
- [3] Darimont, G.L., Cloots, R., Heinen, E., Seidel, L. and Legrand, R., In vivo behavior of hydroxyapatite coatings on titanium implants: a quantitative study in the rabbit. *Biomaterials*, 23(12), pp.2569-2575 (2002).
- [4] Dorozhkin, S.V., Multiphasic calcium orthophosphate ( $\text{CaPO}_4$ ) bioceramics and their biomedical applications. *Ceramics International*, 42(6), pp.6529-6554 (2016).
- [5] da Silva Brum, I., Frigo, L., Dos Santos, P.G.P., Elias, C.N., da Fonseca, G.A.M.D. and de Carvalho, J.J., Performance of Nano-Hydroxyapatite/Beta-Tricalcium Phosphate and Xenogenic Hydroxyapatite on Bone Regeneration in Rat Calvarial Defects: Histomorphometric, Immunohistochemical and Ultrastructural Analysis. *International Journal of Nanomedicine*, 16, p.3473 (2021).
- [6] Alturki, A.M., Abulyazied, D.E., Taha, M., Abomostafa, H.M. and Youness, R.A., A Study To Evaluate The Bioactivity Behavior And Electrical Properties of Hydroxyapatite/ $\text{Ag}_2\text{O}$ -Borosilicate Glass Nanocomposites For Biomedical Applications. *Journal of Inorganic and Organometallic Polymers and Materials*, pp.1-11(2021).
- [7] Stastny, P., Sedlacek, R., Suchy, T., Lukasova, V., Rampichova, M. and Trunec, M., Structure degradation and strength changes of sintered calcium phosphate bone scaffolds with different phase structures during simulated biodegradation in vitro. *Materials Science and Engineering: C*, 100, pp.544-553 (2019). aterials applications. Springer Science & Business Media.
- [8] Wise, D.L., Trantolo, D.J., Altobelli, D.E., Yaszemski, M.J. and Gresser, J.D. eds., *Human*

- biomaterials applications. Springer Science & Business Media (2013).
- [9] Lobo, S.E. and Livingston Arinze, T., Biphasic calcium phosphate ceramics for bone regeneration and tissue engineering applications. *Materials*, 3(2), pp.815-826 (2010).
- [10] Rh. Owen, G., Dard, M. and Larjava, H., Hydroxyapatite/beta-tricalcium phosphate biphasic ceramics as regenerative material for the repair of complex bone defects. *Journal of Biomedical Materials Research Part B: Applied Biomaterials*, 106(6), pp.2493-2512 (2018).
- [11] Li, Y., Ho, J. and Ooi, C.P., Antibacterial efficacy and cytotoxicity studies of copper (II) and titanium (IV) substituted hydroxyapatite nanoparticles. *Materials Science and Engineering: C*, 30(8), pp.1137-1144 (2010).
- [12] Thieme, C., Kracker, M., Thieme, K., Patzig, C., Höche, T. and Rüssel, C., Core-shell structures with metallic silver as nucleation agent of low expansion phases in BaO/SrO/ZnO/SiO<sub>2</sub> glasses. *CrystEngComm*, 21(29), pp.4373-4386 (2019).
- [13] Best, S.M., Porter, A.E., Thian, E.S. and Huang, J., Bioceramics: past, present and for the future. *Journal of the European Ceramic Society*, 28(7), pp.1319-1327 (2008).
- [14] Sivaperumal, V.R., Mani, R., Nachiappan, M.S. and Arumugam, K., Direct hydrothermal synthesis of hydroxyapatite/alumina nanocomposite. *Materials characterization*, 134, pp.416-421(2017).
- [15] Irfan, M. and Irfan, M., Overview of hydroxyapatite; composition, structure, synthesis methods and its biomedical uses. *Biomedical Letters*, 6(1), pp.17-22 (2020).
- [16] Hu, X., Zhang, W. and Hou, D., Synthesis, microstructure and mechanical properties of tricalcium phosphate-hydroxyapatite (TCP/HA) composite ceramic. *Ceramics International*, 46(7), pp.9810-9816 (2020).
- [17] Correa-Piña, B.A., Gomez-Vazquez, O.M., Londoño-Restrepo, S.M., Zubieta-Otero, L.F., Millan-Malo, B.M. and Rodriguez-García, M.E., Synthesis and characterization of nano-hydroxyapatite added with magnesium obtained by wet chemical precipitation. *Progress in Natural Science: Materials International*, 31(4), pp.575-582 (2021).
- [18] Rodríguez-Lugo, V., Karthik, T.V.K., Mendoza-Anaya, D., Rubio-Rosas, E., Villaseñor Cerón, L.S., Reyes-Valderrama, M.I. and Salinas-Rodríguez, E., Wet chemical synthesis of nanocrystalline hydroxyapatite flakes: Effect of pH and sintering temperature on structural and morphological properties. *Royal Society open science*, 5(8), p.180962 (2018).
- [19] Kalita, S.J., Bhardwaj, A. and Bhatt, H.A., Nanocrystalline calcium phosphate ceramics in biomedical engineering. *Materials Science and Engineering: C*, 27(3), pp.441-449 (2007).
- [20] Alobeedallah, H., Ellis, J.L., Rohanizadeh, R., Coster, H. and Dehghani, F., Preparation of nanostructured hydroxyapatite in organic solvents for clinical applications. *Trends Biomater. Artif. Organs*, 25(1), pp.12-19 (2011).
- [21] Chen, F., Wang, Z.C. and Lin, C.J., Preparation and characterization of nano-sized hydroxyapatite particles and hydroxyapatite/chitosan nanocomposite for use in biomedical materials. *Materials letters*, 57(4), pp.858-861 (2002).
- [22] Hwang, K., Song, J., Kang, B. and Park, Y., Sol-gel derived hydroxyapatite films on alumina substrates. *Surface and Coatings Technology*, 123(2-3), pp.252-255 (2000).
- [23] Jang, J.H., Oh, B. and Lee, E.J., Crystalline hydroxyapatite/graphene oxide complex by low-temperature sol-gel synthesis and its characterization. *Ceramics International*, 47(19), pp.27677-27684 (2021).
- [24] Yousefi, K. and Khalife, A., Influence of phosphor precursors on the morphology and purity of sol-gel-derived hydroxyapatite nanoparticles. *Advances in Applied NanoBio-Technologies*, 2(2), pp.49-52 (2021).
- [25] Feng, W., Mu-Sen, L., Yu-Peng, L. and Yong-Xin, Q., A simple sol-gel technique for preparing hydroxyapatite nanopowders. *Materials Letters*, 59(8-9), pp.916-919 (2005).
- [26] Liu, D.M., Troczynski, T. and Tseng, W.J., Aging effect on the phase evolution of water-based sol-gel hydroxyapatite. *Biomaterials*, 23(4), pp.1227-1236 (2002).
- [27] Sargazi, G., Afzali, D., Mostafavi, A. and Kazemian, H., A novel composite derived from a metal organic framework immobilized within electrospun nanofibrous polymers: An efficient methane adsorbent. *Applied Organometallic Chemistry*, 34(3), p.e5448 (2020).
- [28] Kahkha, M.R.R., Kaykhai, M., Sargazi, G. and Kahkha, B.R., Determination of nicotine in saliva, urine and wastewater samples using tantalum metal organic framework pipette tip

- micro-solid phase extraction. *Analytical Methods*, 11(48), pp.6168-6175 (2019).
- [29] Jacobs, A., Gaulier, M., Duval, A. and Renaudin, G., Silver Doping Mechanism in Bioceramics—From Ag<sup>+</sup>: Doped HAp to Ag<sup>0</sup>/BCP Nanocomposite. *Crystals*, 9(7), p.326 (2019).
- [30] Tonsuaadu, K., Gross, K.A., Plüduma, L. and Veiderma, M., A review on the thermal stability of calcium apatites. *Journal of Thermal Analysis and Calorimetry*, 110(2), pp.647-659 (2012).
- [31] Vecstaudza, J., Gasik, M. and Locs, J., Amorphous calcium phosphate materials: Formation, structure and thermal behaviour. *Journal of the European Ceramic Society*, 39(4), pp.1642-164 (2019).
- [32] Bezzi, G., Celotti, G., Landi, E., La Torretta, T.M.G., Sopyan, I. and Tampieri, A., A novel sol-gel technique for hydroxyapatite preparation. *Materials Chemistry and Physics*, 78(3), pp.816-824 (2003).
- [33] Anee, T.K., Ashok, M., Palanichamy, M. and Kalkura, S.N., A novel technique to synthesize hydroxyapatite at low temperature. *Materials Chemistry and Physics*, 80(3), pp.725-730 (2003).
- [34] Sargazi, G., Afzali, D., Mostafavi, A. and Kazemian, H., A novel composite derived from a metal organic framework immobilized within electrospun nanofibrous polymers: An efficient methane adsorbent. *Applied Organometallic Chemistry*, 34(3), p.e5448 (2020).
- [35] Agrawal, K., Singh, G., Puri, D. and Prakash, S., Synthesis and characterization of hydroxyapatite powder by sol-gel method for biomedical application. *J. Miner. Mater. Charact. Eng.*, 10(8), pp.727-734 (2011).
- [36] Stookey, S.D., mColoration of glass by gold, silver, and copper. *Journal of the American Ceramic Society*, 32(8), pp.246-249 (1949).
- [37] de Groot, K., *Ceramics of calcium phosphate: preparation and properties* (pp. 100-114) (1983). CRC Press, Boca Raton, FL.
- [38] Kamiya, K., Yoko, T., Tanaka, K. and Fujiyama, Y., Growth of fibrous hydroxyapatite in the gel system. *Journal of materials science*, 24(3), pp.827-832. 32 (1989).
- [39] Wu, J.M. and Yeh, T.S., Sintering of hydroxylapatite-zirconia composite materials. *Journal of materials science*, 23(10), pp.3771-3777 (1988).
- [40] Zhou, J., Zhang, X., Chen, J., Zeng, S. and De Groot, K., High temperature characteristics of synthetic hydroxyapatite. *Journal of materials science: materials in medicine*, 4(1), pp.83-85.5 (1993).
- [41] Raynaud, S., Champion, E., Bernache-Assollant, D. and Thomas, P., Calcium phosphate apatites with variable Ca/P atomic ratio I. Synthesis, characterization and thermal stability of powders. *Biomaterials*, 23(4), pp.1065-1072 (2002).
- [42] Okazaki, M., Aoba, T., Doi, Y., Takahashi, J. and Moriwaki, Y., Solubility and crystallinity in relation to fluoride content of fluoridated hydroxyapatites. *Journal of dental research*, 60(4), pp.845-849 (1981).
- [43] Okazaki, M., Moriwaki, Y., Aoba, T., Doi, Y. and Takahashi, J., Solubility behavior of CO<sub>3</sub> apatites in relation to crystallinity. *Caries Research*, 15(6), pp.477-483 (1981).
- [44] Fulmer, M.T., Ison, I.C., Hankermayer, C.R., Constantz, B.R. and Ross, J., Measurements of the solubilities and dissolution rates of several hydroxyapatites. *Biomaterials*, 23(3), pp.751-755 (2002).
- [45] Pleshko, N., Boskey, A. and Mendelsohn, R., Novel infrared spectroscopic method for the determination of crystallinity of hydroxyapatite minerals. *Biophysical journal*, 60(4), pp.786-793 (1991).
- [46] Meejoo, S., Maneeprakorn, W. and Winotai, P., Phase and thermal stability of nanocrystalline hydroxyapatite prepared via microwave heating. *Thermochimica acta*, 447(1), pp.115-120 (2006).
- [47] Destainville, A., Champion, E., Bernache-Assollant, D. and Laborde, E., Synthesis, characterization and thermal behavior of apatitic tricalcium phosphate. *Materials Chemistry and Physics*, 80(1), pp.269-277 (2003).
- [48] Zakeri, M., Rahimipour, M.R. and Jamal Abbasi, B., Mechanochemical synthesis of nanocrystalline hydroxyapatite via mechanical alloying. *Materials Technology*, 28(3), pp.159-164 (2013).
- [49] Termine, J.D. and Posner, A.S., Infra-red determination of the percentage of crystallinity in apatitic calcium phosphates. *Nature*, 211(5046), pp.268-270 (1966).
- [50] Ferraz, M.P., Monteiro, F.J. and Manuel, C.M., Hydroxyapatite nanoparticles: a review of

- preparation methodologies. *Journal of Applied Biomaterials and Biomechanics*, 2(2), pp.74-80 (2004).
- [51] Hing, K.A., Gibson, I.R., Di-Silvio, L., Best, S.M. and Bonfield, W., Effect of variation in Ca: P ratio on cellular response of primary human osteoblast-like cells to hydroxyapatite-based ceramics. In *BIOCERAMICS-CONFERENCE-* (Vol. 11, pp. 293-296) (1998).
- [52] Kim, H.M., Himeno, T., Kawashita, M., Kokubo, T. and Nakamura, T., The mechanism of biomineralization of bone-like apatite on synthetic hydroxyapatite: an in vitro assessment. *Journal of the Royal Society Interface*, 1(1), pp.17-22 (2004).
- [53] Kumar, V.B., Khajuria, D.K., Karasik, D. and Gedanken, A., Silver and gold doped hydroxyapatite nanocomposites for enhanced bone regeneration. *Biomedical Materials*, 14(5), p.055002 (2019).